

Surprise in simplicity: an unusual spectral evolution of a single pulse GRB 151006A

R. Basak^{1,2,3*}, S. Iyyani^{4†}, V. Chand⁵, T. Chattopadhyay⁶, D. Bhattacharya⁴, A. R. Rao⁵, S.V. Vadawale⁷

¹ *The Oskar Klein Centre for Cosmoparticle Physics, AlbaNova, SE-106 91 Stockholm, Sweden*

² *Department of Physics, KTH Royal Institute of Technology, AlbaNova University Center, SE-106 91 Stockholm, Sweden*

³ *Nicolaus Copernicus Astronomical Center, Polish Academy of Sciences, Bartycka 18, 00-716 Warsaw, Poland*

⁴ *Inter University Center for Astronomy & Astrophysics, Pune, India*

⁵ *Department of Astronomy and Astrophysics, Tata Institute of Fundamental Research, Homi Bhabha Road, Mumbai, India*

⁶ *Dept. of Astronomy & Astrophysics, Pennsylvania State University, University Park, PA 16802, USA*

⁷ *Physical Research Laboratory, Ahmedabad, India*

Submitted 2017 February 10

ABSTRACT

We present a detailed analysis of GRB 151006A, the first GRB detected by Astrosat CZT Imager (CZTI). We study the long term spectral evolution by exploiting the capabilities of *Fermi* and *Swift* satellites at different phases, which is complemented by the polarization measurement with the CZTI. While the light curve of the GRB in different energy bands show a simple pulse profile, the spectrum shows an unusual evolution. The first phase exhibits a hard-to-soft (HTS) evolution until $\sim 16 - 20$ s, followed by a sudden increase in the spectral peak reaching a few MeV. Such a dramatic change in the spectral evolution in case of a single pulse burst is reported for the first time. This is captured by all models we used namely, Band function, Blackbody+Band and two blackbodies+power law. Interestingly, the *Fermi* Large Area Telescope (LAT) also detects its first photon (> 100 MeV) during this time. This new injection of energy may be associated with either the beginning of afterglow phase, or a second hard pulse of the prompt emission itself which, however, is not seen in the otherwise smooth pulse profile. By constructing Bayesian blocks and studying the hardness evolution we find a good evidence for a second hard pulse. The *Swift* data at late epochs ($> T_{90}$ of the GRB) also shows a significant spectral evolution consistent with the early second phase. The CZTI data (100–350 keV), though having low significance (1σ), show high values of polarization in the two epochs (77% to 94%), in agreement with our interpretation.

Key words: gamma-ray burst: general – radiation mechanisms: non-thermal – radiation mechanisms: thermal – methods: data analysis – methods: observational – methods: statistical.

1 INTRODUCTION

Gamma-ray bursts (GRB) are the most intense cosmological explosions marking the formation of the stellar mass compact objects (Mészáros 2006). The central engine most probably launches a highly relativistic bipolar jet that releases most of the burst energy in a few seconds to a few minutes mostly as gamma-rays, known as the prompt emission (Piran 2004). The surrounding material heated by the outflow glows afterwards on a much longer timescale of days to months, known as the afterglow. As the prompt emission occurs

close to the burst site, it carries the most important signature of the intrinsic properties of the outflowing plasma and the central engine.

The non thermal GRB spectral shape is primarily described by emission processes like, optically thin synchrotron emission (Tavani 1996; Rees & Mészáros 1994; Sari, Piran & Narayan 1998), inverse Compton scattering (Ghisellini & Celotti 1999; Ghisellini et al. 2000). The non-thermal models alone, however, face difficulties in explaining many spectral features across the GRB catalog, such as the hard low energy spectral slopes, collection of the spectral peaks within a small energy range of a few hundred keV and the high efficiency in the production of the observed gamma rays. This leads to the inclusion of thermal emission from the photosphere (Crider et al. 1997; Ghirlanda, Celotti & Ghisellini 2003; Ryde 2004, 2005), thereby representing the very standard fireball

* E-mail: rupal.basak@gmail.com, rupal@camk.edu.pl

† E-mail: shabnam@iucaa.in

model. The observed emission can be entirely from the photosphere wherein the broadness is contributed by the continuous or localised subphotospheric dissipation of the kinetic energy or Poynting flux (Beloborodov 2010, 2013; Giannios 2012; Pe'er, Mészáros & Rees 2005; Rees & Mészáros 2005; Iyyani et al. 2015), or may be due to the geometrical effects of the jet emission and its structure (Lundman, Pe'er & Ryde 2013; Beloborodov 2011; Basak & Rao 2015a). Or, the photospheric emission can be a sub-dominant component (Burgess et al. 2014; Axelsson et al. 2012; Iyyani et al. 2013; Guiriec et al. 2011, 2013). All the models have certain pros and cons and confront issues in justifying the constraints obtained from observations. The radiation processes of the prompt emission, thus, remains the most debated topic in the GRB field (see Zhang 2014; Kumar & Zhang 2015; Pe'er 2015 for recent reviews).

On the other hand, the spectral analysis of the prompt emission itself is challenging because of the rapid spectral evolution and multiple pulse emission which may have large overlaps. Several studies conducted for GRBs with single/separable pulses show definite evolution of the spectral peak (E_p), either hard to soft (HTS) or intensity tracking (IT) (Liang & Kargatis 1996; Kaneko et al. 2006; Lu et al. 2012; Basak & Rao 2014). However, for GRBs with overlapping pulses, this picture is complicated which is probably affected by pulse overlap (e.g., Hakkila & Preece 2014). Also, a GRB detector having an unavoidable wide field of view, is background limited and suffers from poor spectral sensitivity.

The spectral study of the prompt emission has been revolutionized in the past two decades particularly after the launch of the *Swift* and the *Fermi* satellites. The GRB Monitor (GBM) and the Large Area Telescope (LAT) of the *Fermi* provide seven decades of energy band ranging from 8 keV to ~ 200 GeV, (see Meegan et al. 2009; Atwood et al. 2009). The *Swift* Burst Alert Telescope (BAT) being a coded-mask instrument provides a good localization and background estimate in 15–150 keV, while the X-ray Telescope (XRT) covers the lower energy range of 0.3–10 keV. The localization accuracy of both together with the fast re-pointing capability of the spacecraft facilitates the redshift measurements for the majority of GRBs, see Gehrels et al. (2004); Burrows et al. (2005). It has been suggested that the focusing instruments like the XRT, having a better sensitivity and spectral resolution than the wide-field detectors, can be used at the late epochs to identify any additional spectral component with a good statistical significance (Basak & Rao 2015a). The novel strategy here is to exploit the specific ability of individual detectors at different phases of a GRB, namely, the wide band *Fermi* data at the early phase, complemented by the finest spectral data of the XRT at the late prompt and/or early afterglow phase (Basak & Rao 2015a) and thereby studying the spectral evolution until the late epochs. For even longer GRBs, e.g., the ultra-long ones, it is also possible to observe them with highly sensitive detectors of *Chandra* and wide band as well as fine spectral resolution detectors of *NuSTAR* (Basak & Rao 2015b).

Another important addition to these studies would be the polarization which can be used as a diagnostic tool between different models. The first such detection was reported for GRB 021206 (linear polarization degree, $\Pi = 80 \pm 20\%$), detected by *Reuven Ramaty High Energy Solar Spectroscopic Imager (RHESSI)* (Coburn & Boggs 2003, however, see Rutledge & Fox 2004; Wigger et al. 2004). This was followed by e.g., *INTEGRAL* observation (100 keV – 1 MeV) of GRB 041219A and GRB 061122, Kalemci et al. (2007); McGlynn et al. (2007); Götz et al. (2009, 2013), *IKAROS*/gamma ray burst polarimeter (GAP) observation of GRB 100826A ($\Pi = 25 \pm 15\%$ and $31 \pm 21\%$ in different time intervals),

Table 1. Observation of GRB 151006A with different detectors. Time is counted since the GBM trigger

Detector	Time bins	Time interval (s)
GBM	1–14	–2.0 – 88.1
LAT-LLE	1–9	–2.0 – 27.5
LAT (> 100 MeV)	8 and 11	16 – 20, 37 – 53
BAT	15–18	88.2 – 253.2
XRT	from bin 12	> 58.5

GRB 110721A ($\Pi = 84^{+16}_{-28}\%$) and GRB 110301A ($\Pi = 70 \pm 22\%$), see Yonetoku et al. (2011, 2012).

High polarization degree is generally owed to the observed non-thermal emission. Several theoretical models have been proposed such as Compton drag (Lazzati et al. 2004), synchrotron emission in ordered magnetic fields (Nakar, Piran & Waxman 2003; Granot & Königl 2003) as well as in random magnetic fields (Waxman 2003). On the other hand, photospheric emission in general is thought to be unpolarised, however, the photospheric emission (blackbody alone) from a structured jet, observed off axis is predicted to show a polarization degree up to $\Pi = 40\%$ (Beloborodov 2011; Lundman, Pe'er & Ryde 2014). In case of subphotospheric dissipation models, polarised emission is expected to be observed in soft X-rays from synchrotron emission when dissipation occurs close to the photosphere. The MeV peak and spectrum above the peak is not expected to be polarised as they are formed at high optical depths (Lundman, Vurm & Beloborodov 2016). In order to have a significant polarization detection, the crucial factor is to have high photon statistics, which has been a concern in most of the polarization measurements.

The CZTI Imager (CZTI), on-board the recently launched multi-wavelength Indian mission *Astrosat*, provides detection in the energy range 20 – 200 keV and becomes an open detector above 100 keV, thereby enabling it to detect GRB events. The Veto detector when augmented, raises the detection energy level to 600 keV. Thus, when analysed along with the BAT data, the CZTI + Veto will become crucial in constraining the spectral peak energies, which is otherwise not generally possible with the BAT data alone (Rao et al. 2016). The CZTI also possesses X-ray polarization detection capabilities in the energy range, 100 – 380 keV (Vadawale et al. 2015). Thus, with its wide field of view, good spectral resolution and polarimetry capability, the CZTI data will be a key addition to the existing observatories like the *Swift* and *Fermi*.

In this paper, we present a detailed study of spectral evolution of GRB 151006A, the first detected GRB by the CZTI. We follow the strategy of multi-instrument analysis using the detectors on-board *Fermi* and *Swift* at different phases of GRB emission. This is further complemented by the polarization data from the CZTI. The paper is organized as follows. Section 2 presents the observation by various instruments, the methodology of the data analysis and the spectral models used; section 3 presents the results of the spectral fits and the polarization measured by CZTI, finally followed by conclusions and a discussion in Section 4.

2 OBSERVATIONS AND DATA ANALYSIS

On 2015 October 06 at 09:54:57.83 UT, the *Fermi*/GBM (Roberts & Meegan 2015) triggered on GRB 151006A. The burst also triggered many other detectors including the *Swift*/BAT at 09:55:01 UT (Kocevski et al. 2015), the *Astrosat*/CZTI (Bhalerao et al. 2015)

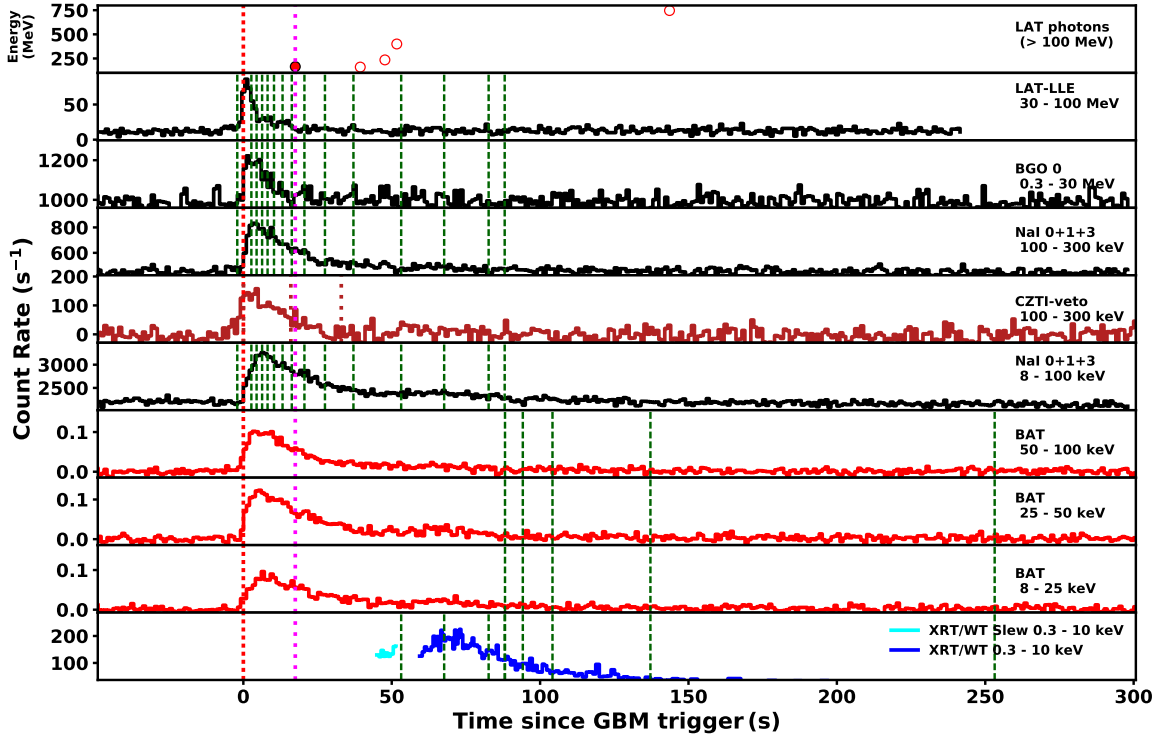


Figure 1. Light curve of GRB 151006A extracted from the *Fermi*, *Astrosat*/CZTI and *Swift* at different energies (labeled in the respective panels). The time intervals chosen for our analysis are shown by dashed lines. We also mark the GBM trigger time with dot-dashed red line (at $t = 0$) and the first LAT photon detection time with a vertical magenta line with horizontal dashes (at $t = 17.5$ s). The time intervals for polarization measurements (0–16 s and 16–33 s) are marked in the CZTI-veto panel with dotted brown line.

at 09:54:57.825 UTC, Konus-Wind at 09:54:57.7 UT (Golenetskii et al. 2015) and CALET at 09:54:59.97 UT (Yoshida et al. 2015).

In the current paper, we present the spectral analysis of *Fermi* and *Swift* data, and the polarization measurement obtained from CZTI data. Figure 1 shows a composite count rate light curve of various detectors on-board the *Fermi*, *Swift*, and the CZTI of *Astrosat* arranged from higher to lower energy bands. These are LAT (P8_SOURCE class events, > 100 MeV), LAT Low energy events (LLE, 30 MeV–100 MeV), GBM/BGO detector (300 keV–30 MeV), GBM/NaI detectors (100–300 keV), CZTI-veto (100–300 keV), GBM/NaI detectors (8–100 keV), followed by the *Swift* BAT in 50–100 keV, 25–50 keV, 15–25 keV and the *Swift* XRT (0.3–10 keV). The GBM light curve shows a single pulse having a fast rise and an exponential decay (FRED) with a duration (T_{90}) of ~ 84 s (50–300 keV) (Roberts & Meegan 2015). The LLE emission of the burst is coincident with the GBM trigger and peaks simultaneously with the BGO emission at ~ 1.4 s. The LLE emission is quite significant with a detection sigma of 54, and extends for about ~ 30 s (Ohno et al. 2015). The emission consists of a narrow pulse accompanied by two other smaller pulses towards the end. Thus, LLE emission does not show the typical delay that is observed in its onset with respect to the GBM observations (Ackermann et al. 2013). The LAT LLE data bridges the gap between the BGO and LAT detections, and thereby helps in constraining high MeV spectral peaks (Axelsson et al. 2012; Moretti & Axelsson

2016). However, the LAT (P8R2_source class events, > 100 MeV) events are observed to arrive only 17.5 s after the GBM trigger. The LAT emission is less significant with only 5 photons detected in total. The top panel of Fig. 1 shows the photons to be associated to the GRB with probability > 0.9 in red filled circle, otherwise in open circles (using `GTSRCPROB` of *Fermi* science tool¹). The delayed onset of the LAT events with respect to GBM emission is consistent with that observed for long bursts as reported in Ackermann et al. (2013). We note that high energy emission in the energy range, 100 keV – 30 MeV and 30 MeV – 100 MeV, peaks nearly simultaneously at ~ 1.4 s, whereas the low energy emission in the energy range, 8 keV - 100 keV, peaks later at ~ 5.4 s. The BAT light curve also shows a single FRED like pulse with a T_{90} (15–350 keV) of 203.9 ± 41.6 s (Cummins et al. 2015). The XRT started observations nearly 48.6 s after the BAT trigger and located an X-ray source at RA = 147.43 d and DEC = 70.5 d. The XRT observed in Window Timing (WT) mode during 55.3–570.8 s, and in photon counting mode afterwards until 114 ks (both the time counted from the BAT trigger time). The long term XRT light curve is best fitted with a double-broken power law with slopes of $-0.5^{+0.2}_{-2}$ until 91 s, -2.1 ± 0.4 until 134 s and -1.39 ± 0.02 afterwards (XRT repository; Evans et al. 2009). In the current analysis we have included

¹ <http://fermi.gsfc.nasa.gov/ssc/data/analysis/scitools/overview.html>

the XRT data only until ~ 600 s, i.e the part with WT mode observation and nearly coincident with the observed BAT emission.²

GRB 151006A was also the first GRB detected by the *Astrosat* CZTI, on its first day of operation (Bhalerao et al. 2015; Rao et al. 2016). Both CZTI and Veto detector light curves also show a single FRED like pulse in both the energy ranges 50–200 keV and 100–500 keV, see Figure 2 in Rao et al. (2016).

For the spectral study with the *Fermi*/GBM, we choose three NaI detectors having the highest count rate, namely n0, n1 and n3, where the numbering of the NaI detectors follows the usual convention, i.e., ‘nx’ with $x = 0 - 11$. As the number of all the NaI detectors are within $x \leq 5$, we choose the BGO number b0, where ‘by’ denotes a BGO detector with $y = 0 - 1$. We then use Fermi Burst Analysis GUI v 02-01-00p1 (GTBURST³) to extract the spectrum. As the n3 has the highest count rate among the chosen NaI detectors, we use it to define the time intervals for time resolved spectroscopy. We apply a signal-to-noise ratio (S/N) of 20 and find 14 time bins in the interval $-2.0 - 88.1$ s. The LAT LLE data is also extracted in these time bins until ~ 27 s, following the standard procedure described in Ackermann et al. (2013). The LAT P8R2_source class events, > 100 MeV, events were selected within a 12 deg region centred around the *Swift* XRT position. Among the 5 detected LAT photons, only 4 arrive during the GBM T_{90} of the burst. Thus, for the temporal analysis, depending on the availability of the data, the LAT spectra is extracted in the energy range, 100 MeV – 1 GeV, only for time intervals: 16.3 - 20.5 s (bin 8) and 37 -53 s (bin 11).

The first 88 s of the *Fermi* data is augmented by the observation with the *Swift*/BAT (88 – 253 s) and *Swift*/XRT at later times (> 58.5 s). The data of the BAT was extracted following the standard procedure. The data is calibrated using the task BATECONVERT, followed by constructing a detector plane image using BATBINEVT. The known bad detectors and the noisy pixels are eliminated by BATDETMASK and BATHOTPIX. It is then mask weighted by BATMASKWTEVT. Finally, the spectrum is extracted with BATBINEVT in a specified time interval. The spectrum is corrected by ray-tracing with BATUPDATEPHAKW and the response matrix is generated using BATDRMGEN. The XRT data was extracted using the standard tools provided by the UK Swift Science Data Centre (Evans et al. 2009)⁴. We extract the spectrum from the WT data with a pileup and exposure map correction.

As for the spectral model, we first choose Band function (Band et al. 1993), which is a broken power law with two photon indices, α and β and a peak, E_p in the νF_ν representation. A majority of GRB data is consistent with this function (e.g., Gruber et al. 2014; Goldstein et al. 2013). As we will show in Section 3.1, the evolution of the E_p of the Band function with time shows a sudden jump. As GRB spectrum has been found to have multiple spectral components, this sudden jump can as well represent another peak in the spectrum which is not captured by the single peak Band function. In order to check that the spectral variation is real, we then use two models, Band function + Blackbody (Band + BB), e.g., Guiriec et al. (2011); Axelsson et al. (2012); Guiriec et al. (2013) and Two blackbodies + power law (2BB + PL), e.g., Basak & Rao (2014, 2015a); Iyyani et al. (2015). In addition, at the later phase where

the data does not allow to put a constrain on the high energy power law, we use instead a blackbody + power law (BB + PL) model.

The spectral analysis is carried out in XSPEC version: 12.9.0. For the analysis involving *Fermi*/GBM and LAT data, PG-Statistic is used (Greiner et al. 2016) and that involving *Swift*/BAT and XRT data, χ^2 statistic⁵ is used. All the errors on the fit parameters are quoted at 1σ (nominal 68% confidence).

2.1 Effective area correction:

The different detectors used for the spectral analysis are expected to have some differences in the calibration. We multiply a constant factor for each detector used for a spectral fitting for the effective area correction (EAC). However, as each time-resolved data has a limited number of counts, the EAC constant may not be well constrained. Hence, we adopt the following procedure.

First, note that it is sufficient to determine the correction factor of all the detectors relative to one of the detectors. Hence, we freeze the EAC constant value corresponding to the detector having the highest count rate to 1, while that of the other detectors are made free. We then load the time-resolved data of all the detectors in all the time bins simultaneously. Then the EAC constant parameter of the individual detectors are linked throughout all the time bins. For example, let us assume that we have three detectors and four time bins, with detector 1 having the highest count rate. We load $3 \times 4 = 12$ data groups simultaneously. Group 1–3 correspond to time bin 1, group 4–6 correspond to time bin 2 and so on. Now, the constant parameter of group 1 is fixed to 1, while that of group 2 and 3 are free. From the next time bin onward this parameter is linked to the corresponding value of time bin 1. Thus, the constant parameter of the group 4 is set equal to that of the group 1, that of the group 5 is set equal to that of the group 2, and so on. Note that this procedure is allowed as the EAC of the detectors cannot vary with time. On the other hand, linking this parameter throughout all the time bins enable us to determine the value with much higher accuracy than that obtained by individual fits.

In the present study, as the n3 detector has the highest count rate, we freeze the EAC constant of this to 1. As the LAT-LLE data is available until bin 9, we use the procedure until this time bin. For the various models we use, we find that the EAC constant of all the detectors of GBM give quite similar values. These are — n3: 1 (fixed), n0: 0.95 ± 0.03 , n1: 0.93 ± 0.03 , b0: 1.0 ± 0.1 . The EAC constant corresponding to the LAT-LLE was found to widely differ between models. The value is sometimes unrealistically low (< 0.3). Based on the current understanding of the different detectors of the *Fermi*, the EAC constant factor is not expected to differ by more than 30%. We find that the Band + BB gives the most realistic value of this factor in the range 0.40–1.02. Note that due to much less number of spectral bins, the constant factor is not well constrained even after using the above mentioned procedure. As the value is consistent with having no correction, we freeze the EAC constant factor corresponding to the LAT-LLE and the LAT data (> 100 MeV) to 1 for all spectral fitting. For the XRT analysis, we find the constant factor in the range 0.8–1.2, and hence, we freeze it to 1. We do not apply any cross-calibration between the XRT and the BAT.

² For a full light curve of the XRT observations, please refer to the online repository in the link http://www.swift.ac.uk/xrt_curves/00657750/

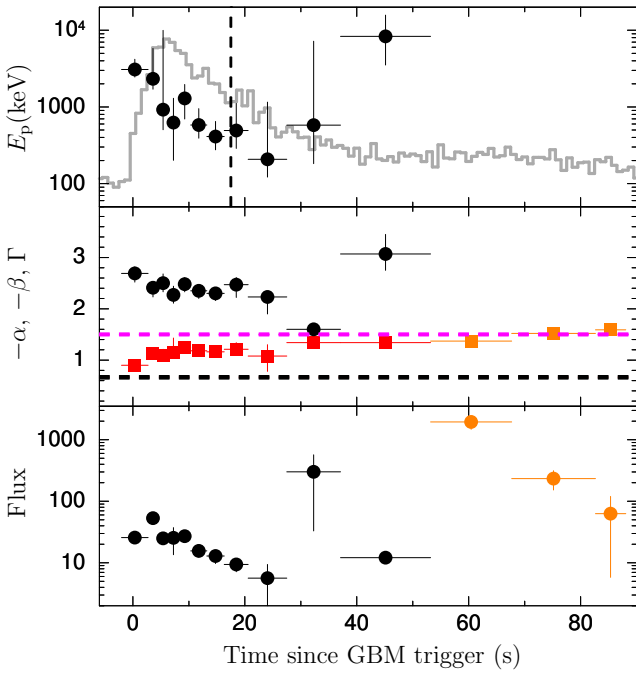
³ <http://fermi.gsfc.nasa.gov/ssc/data/analysis/scitools/gtburst.html>

⁴ http://www.swift.ac.uk/burst_analyser/

⁵ http://swift.gsfc.nasa.gov/analysis/bat_swguide_v6_3.pdf

Table 2. Parameters of time resolved spectral fitting with Band model. Bin 8 and 11 have a simultaneous coverage with the LAT data marked ^(a)

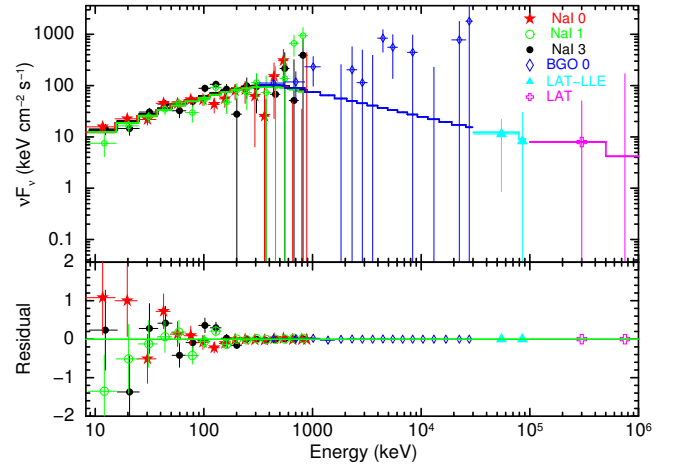
Bin #	Time interval (s)	α	β	E_{peak} (keV)	N_{Band} (10^{-3})	PG-Stat (dof)
1	−2.0 – 2.7	$-0.90^{+0.05}_{-0.06}$	$-2.7^{+0.1}_{-0.2}$	3082^{+1110}_{-631}	$3.4^{+0.2}_{-0.2}$	489.8 (477)
2	2.7 – 4.5	$-1.13^{+0.04}_{-0.05}$	$-2.4^{+0.1}_{-0.2}$	2325^{+3475}_{-520}	$10.9^{+0.4}_{-0.5}$	457.2 (477)
3	4.5 – 6.3	$-1.10^{+0.11}_{-0.04}$	$-2.5^{+0.2}_{-0.2}$	921^{+9036}_{-416}	$12.3^{+2.0}_{-0.6}$	532.3 (477)
4	6.3 – 8.2	$-1.14^{+0.29}_{-0.09}$	$-2.3^{+0.2}_{-0.2}$	625^{+670}_{-424}	$13.3^{+7.7}_{-1.5}$	499.2 (477)
5	8.2 – 10.3	$-1.25^{+0.10}_{-0.03}$	$-2.5^{+0.1}_{-0.2}$	1292^{+669}_{-370}	$10.5^{+1.4}_{-0.4}$	507.8 (477)
6	10.3 – 13.2	$-1.18^{+0.09}_{-0.08}$	$-2.4^{+0.1}_{-0.2}$	582^{+396}_{-191}	$9.9^{+1.3}_{-1.1}$	471.2 (477)
7	13.2 – 16.3	$-1.16^{+0.11}_{-0.09}$	$-2.3^{+0.1}_{-0.1}$	411^{+237}_{-135}	$10.1^{+1.8}_{-1.3}$	529.5 (477)
8 ^(a)	16.3 – 20.6	$-1.21^{+0.13}_{-0.12}$	$-2.5^{+0.1}_{-0.2}$	492^{+619}_{-304}	$7.6^{+1.7}_{-1.3}$	574.9 (487)
9	20.6 – 27.5	$-1.08^{+0.22}_{-0.30}$	$-2.2^{+0.1}_{-0.3}$	208^{+950}_{-86}	$7.3^{+3.3}_{-2.9}$	612.8 (477)
10	27.5 – 37.1	$-1.34^{+0.16}_{-0.10}$	$-1.6^{+0.1}_{-0.1}$	580^{+6619}_{-397}	$3.1^{+0.8}_{-0.4}$	640.5 (469)
11 ^(a)	37.1 – 53.2	$-1.34^{+0.06}_{-0.06}$	$-3.1^{+0.4}_{-0.3}$	8318^{+7462}_{-4801}	$1.6^{+0.1}_{-0.1}$	747.4 (479)


Figure 2. Evolution of the parameters of the Band model fitted to the time-resolved *Fermi*/GBM, LAT and XRT data. For Bin 12–14, we show the parameters of the power law model fits in orange symbols. Top to bottom — Panel 1: E_p ; Panel 2: Photon index α (red filled boxes), β (black filled circles) of the Band function, and the power law index, Γ (orange filled boxes); Panel 3: Energy flux in units of 10^{-7} erg cm^{-2} s^{-1} . The light curve in energy range, 8 keV – 100 keV, is shown in gray in Panel 1. The detection of the first LAT photon at 17.5 s is marked by a vertical dashed line in Panel 1. In Panel 2, the synchrotron fast cooling photon index of 3/2 and the slow cooling photon index of 2/3 are marked by horizontal dashed lines.

3 RESULTS

3.1 Spectral evolution during the prompt emission

The results of the Band fits are shown in Table 2 and Fig. 2. An example of Band fit is shown for Bin 8, where the wide band data including that of the LAT is available, see Fig. 3. The parameters could be constrained until Bin 11, and afterwards the Band turns to be a single power law. Note that the E_p evolution in Panel 1 of Fig. 2 shows a hard-to-soft (HTS) evolution until Bin 9 and then the value starts to increase and reaches a few MeV. When the spectral evolu-


Figure 3. Wide band spectrum of Bin 8 fitted with the Band function. Markers (and colours) used for different detectors are shown in the legend.

tion is compared with the 8 keV – 100 keV light curve, shown in the background, the evolution does not seem to show an intensity-tracking (IT) trend either. Note from Fig. 1 that none of the light curves in any energy band show any new pulse at this phase. However, interestingly, we note that the first LAT photon (> 100 MeV) arrives at 17.5 s, which is marked by a dashed line in both Fig. 1 and Fig. 2. The observed change in the spectral peak of the Band function takes place during this time. This thereby suggests either an onset of a second hard pulse related to the prompt emission or the beginning of the afterglow phase (see Section 3.3 and Section 4 for a detailed discussion).

In the second panel of Fig. 2, we show the evolution of the photon indices of the Band function as well as that of the power law. Negative values of α and β are shown in order to match the convention of the photon index Γ of the power law model i.e., $N(E) \propto E^{-\Gamma}$. The α values are found to be softer than the line of death of synchrotron emission (Preece et al. 1998) i.e. $\alpha = -0.67$, corresponding to slow cooling synchrotron emission, throughout the burst duration. In accordance to what is typically observed (Kaneko et al. 2006), α is found to get softer with time, tending to values, $\alpha = -1.5$, consistent with fast cooling synchrotron emission (marked as pink horizontal dash line in Fig. 2). The value of β also decreases gradually over time. As a result of which, at later times, it becomes difficult to constrain the spectral peak and spectrum is then modelled by a simple power law. The power law index,

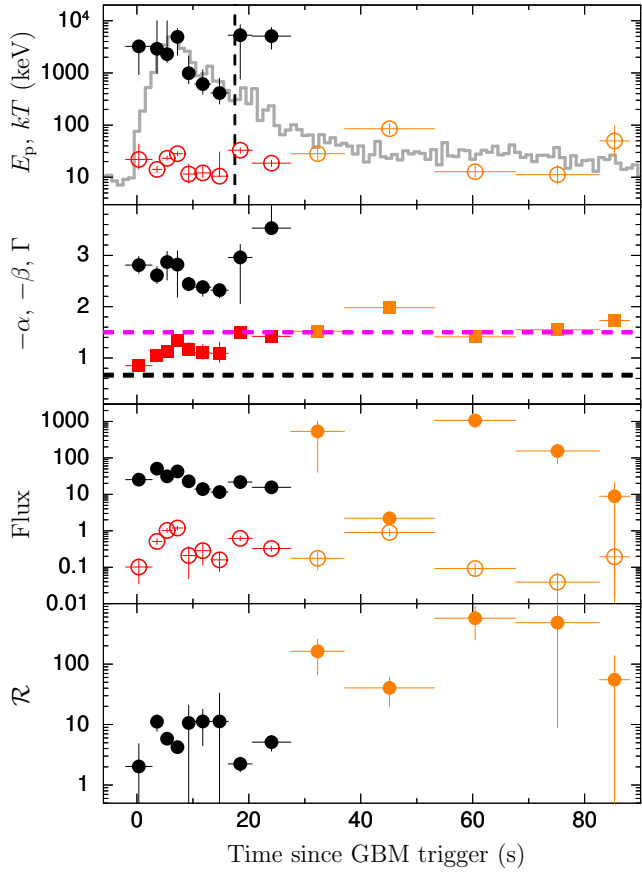


Figure 4. Evolution of the parameters of the Band + BB model fitted to the time-resolved *Fermi*/GBM, LAT and XRT data. For Bin 10–14, the parameters of the BB + PL model fits are shown in orange symbols. From top to bottom — Panel 1: E_p of the Band (black filled circles) and kT of the blackbody (red open circles); Panel 2: Photon index $-\alpha$ (red filled boxes), $-\beta$ (black filled circles) of the Band function, and the power law index, Γ (orange filled boxes); Panel 3: Energy flux in units of 10^{-7} erg cm $^{-2}$ s $^{-1}$ for Band (black filled circles), BB (red open circles) and power law (orange filled circles); Panel 4: \mathcal{R} in units of 10^{-21} . The light curve in energy range, 8 keV - 100 keV, is shown in grey in Panel 1. The detection of the first LAT photon at 17.5 s is marked by a vertical dashed line in Panel 1. In Panel 2, the synchrotron fast cooling photon index of 3/2 and the slow cooling photon index of 2/3 are marked by horizontal dashed lines.

Γ has values equal to 1.5. Such hard values of $\Gamma < 2$ suggest either a spectral peak or cutoff to lie beyond the observed energy window, e.g. González et al. (2003).

In the third panel we show the evolution of bolometric energy flux in 0.1 keV – 100 GeV. We however note that the bolometric value inherently assumes that the same model can be extended in both lower and higher energies. While an observed flux would not have such assumption, it can underestimate the powerlaw flux. Also, as we have used different detectors at different phases of the GRB, the bolometric flux automatically provides a uniform band for all observation. The flux at any desired energy band can be easily calculated using the parameters given in the tables. The Band flux smoothly decreases until bin 9. Note that the power law model as well as in case of the Band function (bin10), where the Band nearly tends to be a power law (β is nearly equal to α), show an increased flux in comparison to the otherwise smooth evolution. This is due to the fact that in other bins, the Band function has a steeper

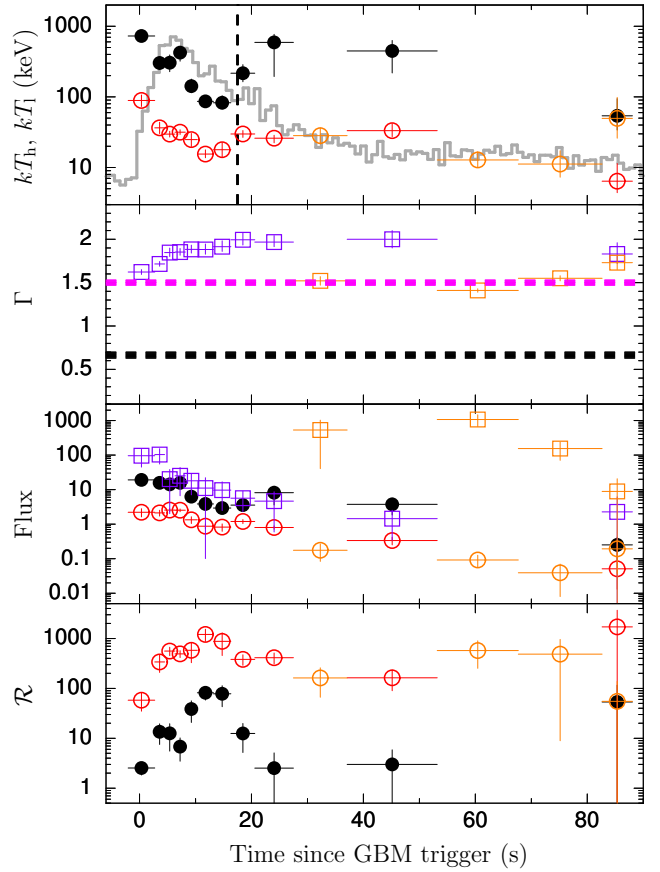


Figure 5. Evolution of the parameters of the 2BB + PL and BB + PL model fitted to the time-resolved *Fermi*/GBM, LAT and XRT data are shown. The parameters of the high energy blackbody, low energy blackbody and the power law component of the 2BB + PL model are shown in black filled circles, red open circles and violet open boxes respectively. The parameters of BB + PL model fits are shown in symbols of orange colour. From top to bottom — Panel 1: Temperature of the blackbodies; Panel 2: Power law photon index, Γ ; Panel 3: Energy flux of each component in units of 10^{-7} erg cm $^{-2}$ s $^{-1}$; Panel 4: \mathcal{R} in units of 10^{-21} . The light curve in energy range, 8 keV - 100 keV, is shown in grey in Panel 1. The detection of the first LAT photon at 17.5 s is marked by a vertical dashed line in Panel 1.

slope at higher energies than the power law which does not have a break. Consequently, in these bins the fluxes are over estimated.

The apparent jump in E_p evolution as found above calls for a detailed study. This is solely a spectral variation as the underlying lightcurve does not show any change. It is known that GRB spectrum can have multiple components with two peaks e.g., Band + BB, or 2BB + PL. If one of the components is dominant, it is possible that our single component Band function picks up that one leading to an artificial E_p variation. Hence, in order to check that the variation is physical we use these two models. The corresponding spectral evolutions are shown in Fig. 4 for Band + BB and Fig. 5 for 2BB + PL model. Whenever the curvature at high energies cannot be constrained, we use the simpler BB + PL model, which these two models would converge to. For the parameters of all the fits, see Appendix A. For bins 12–14, we include simultaneous XRT observation as well. As soft X-rays suffer from absorption at the source and the Galaxy, we include two absorption terms (TBABS in XSPEC) in the model. The equivalent hydrogen column density (n_H) of the Galactic term is fixed to 7.74×10^{20} atoms cm $^{-2}$. Then we

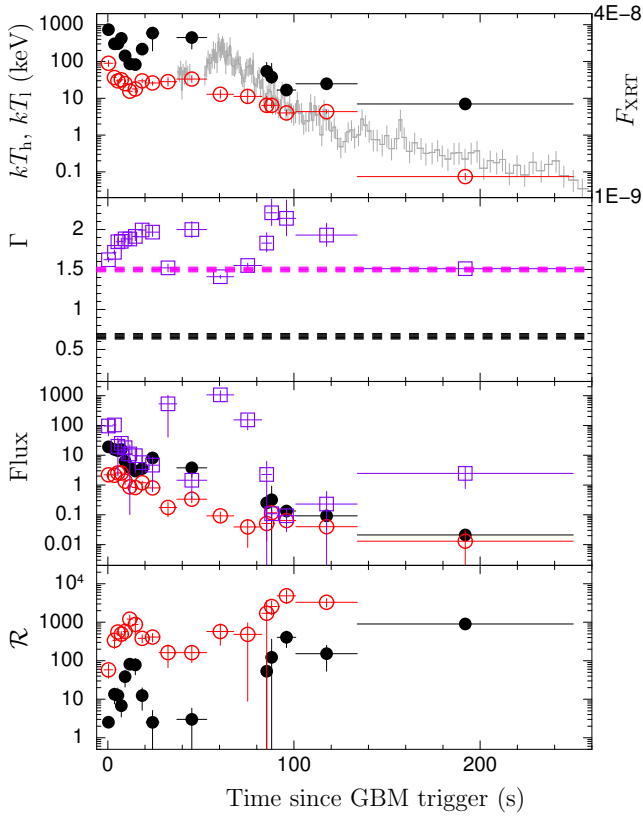


Figure 6. Long time evolution of the parameters of the 2BB + PL model are shown. The symbols used are the same as in Fig. 5. The data after 88 s correspond to Table 3. The 0.3–10 keV XRT flux ($\text{erg cm}^{-2} \text{s}^{-1}$) is shown in the background of Panel 1 and the corresponding vertical scale is shown on the right. The value of \mathcal{R} of the lower-temperature blackbody is not shown for the last time interval, as due to a very low temperature, we obtained an unrealistically high value.

link the n_H of the source absorption term between the time bins. We obtain $n_H = (5.1 \pm 0.6) \times 10^{21} \text{ atoms cm}^{-2}$. For subsequent fitting with the XRT data, we freeze the source n_H at this value as this cannot evolve with time and the linking of the parameter gives good confidence on the obtained value.

From the upper panels of Fig. 4 and Fig. 5 we see a very similar variation of the spectral peak as before. This indeed shows that the sudden jump in the peak energy is not an artefact of the adopted model. The next two panels of the Figures are same as Fig. 2. In the fourth panel, we also show the evolution of the parameter $\mathcal{R} \equiv (F_{BB}/\sigma T^4)^{1/2}$ of the blackbody component. \mathcal{R} represents the effective transverse size of the emitting region (i.e photosphere) provided the bulk Lorentz factor of the outflow, $\Gamma_B \gg 1/\theta_j$ where θ_j is the jet opening angle (Ryde & Pe'er 2009). For Band + BB note that \mathcal{R} does not show a linear increase in contrast to what is typically observed (Ryde & Pe'er 2009; Ryde 2004, 2005), instead only exhibits an overall increment throughout. On the other hand, the variation of \mathcal{R} for both the thermal components of 2BB + PL model exhibit a similar jump corresponding to the evolution of E_p .

3.2 Spectral evolution at late times (> 88 s)

The BAT and XRT spectrum at late times are extracted when the S/N of the *Fermi* does not allow any further time division. The XRT

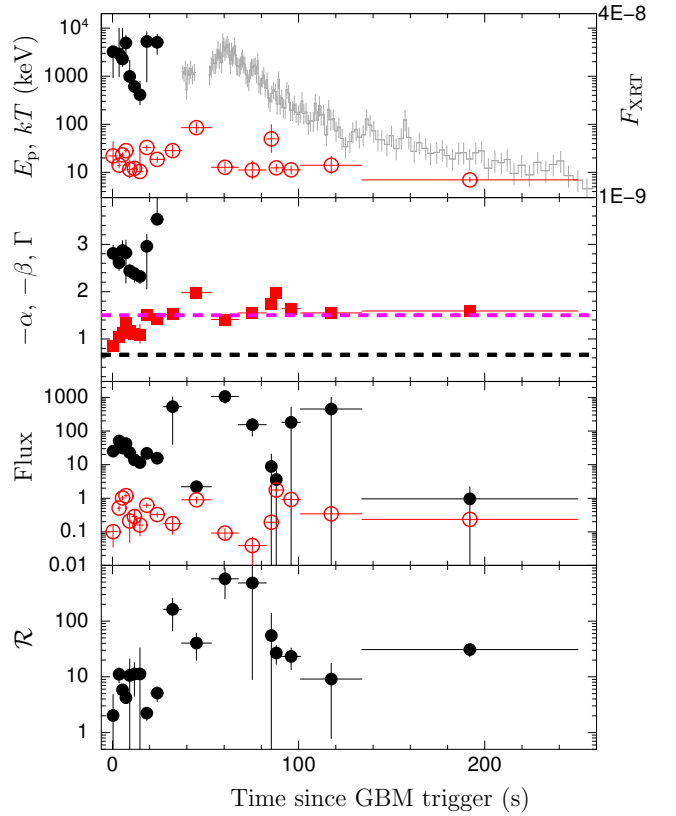


Figure 7. Long time evolution of the parameters of the Band+BB model (Bin 1–9) and BB+PL model (Bin 10–18) are shown. The symbols used are the same as in Fig. 4. The 0.3–10 keV XRT flux ($\text{erg cm}^{-2} \text{s}^{-1}$) is shown in the background of Panel 1 and the corresponding vertical scale is shown on the right.

data in WT mode and the BAT data are available until 570 s and ~ 250 s, respectively. Note that the XRT light curve has two breaks one at 91 s and another at 134 s, both counted with respect to the BAT trigger time. Hence, in choosing the time intervals, we respect these break times and choose roughly logarithmic bins i.e., the interval length increases roughly as a geometric progression. We obtain 5 bins: 85–91 s, 91–101 s, 101–134 s, 134–250 s and 250–570 s (from BAT trigger time). The simultaneous BAT data is extracted in the first four intervals.

The time-resolved data is analysed with a power law (PL), BB + PL, 2BB + PL and Band function. As before, two absorption terms — the Galactic n_H is set to $7.74 \times 10^{20} \text{ atoms cm}^{-2}$ and the source n_H to $5.1 \times 10^{21} \text{ atoms cm}^{-2}$, are used. The result of the fits are shown in Table 3. We find that the PL does not give a good fit (see Table 3) and shows large residual. The spectra are much better fitted with the BB+ PL model and even better with the 2BB + PL model. This shows that there is a curvature in the spectrum. Hence, this phase most probably corresponds to the prompt emission phase. We found that the Band function shows an equally bad fit as the PL model and the E_p could not be constrained. The 2BB + PL model seems to be the best fit at the late time. For the last bin, as the BAT data is no more available we could not constrain the parameters of more complicated models other than the PL in the limited bandwidth of the XRT. Hence, only the results of PL fit is reported for this bin.

In Fig. 6, we show the evolution of the parameters of the 2BB

Table 3. Parameters of time resolved spectral fitting of the joint BAT and XRT data at late times. We also show the χ^2 of the models, including that of the Band function fits.

Bin #	Interval (s)	Model	kT_h (keV)	N_h (10^{-1})	kT_1 or kT (keV)	N_1 (10^{-1})	Γ	N_Γ (10^{-1})	χ^2 (dof)
15	88.2 – 94.2	PL					$1.39^{+0.05}_{-0.05}$	$5.4^{+0.5}_{-0.4}$	113.4 (75)
		BBPL			12^{+2}_{-2}	$2.1^{+0.3}_{-0.3}$	$1.97^{+0.13}_{-0.12}$	$8.4^{+0.8}_{-0.8}$	86.9 (73)
		2BBPL	38^{+52}_{-13}	$3.8^{+13}_{-1.4}$	6^{+1}_{-1}	$1.4^{+0.3}_{-0.3}$	$2.21^{+0.17}_{-0.16}$	$8.9^{+0.8}_{-0.8}$	70.8 (71)
		Band							103.1 (73)
16	94.2 – 104.2	PL					$1.40^{+0.04}_{-0.04}$	$4.6^{+0.3}_{-0.3}$	88.9 (75)
		BBPL			11^{+2}_{-2}	$1.1^{+0.3}_{-0.2}$	$1.64^{+0.11}_{-0.10}$	$5.4^{+0.5}_{-0.5}$	77.8 (73)
		2BBPL	17^{+4}_{-3}	$1.6^{+0.3}_{-0.3}$	4^{+1}_{-1}	$0.8^{+0.2}_{-0.2}$	$2.14^{+0.23}_{-0.22}$	$6.2^{+0.5}_{-0.5}$	70.4 (71)
		Band							82.8 (73)
17	104.2 – 137.2	PL					$1.43^{+0.04}_{-0.03}$	$3.0^{+0.1}_{-0.1}$	89.5 (75)
		BBPL			14^{+8}_{-5}	$0.4^{+0.2}_{-0.2}$	$1.55^{+0.07}_{-0.07}$	$3.2^{+0.2}_{-0.2}$	84.9 (73)
		2BBPL	25^{+10}_{-5}	$1.1^{+0.5}_{-0.3}$	$4.3^{+0.6}_{-0.4}$	$0.5^{+0.1}_{-0.1}$	$1.93^{+0.15}_{-0.14}$	$3.6^{+0.2}_{-0.2}$	72.8 (71)
		Band							77.8 (73)
18	137.2 – 253.2	PL					$1.38^{+0.04}_{-0.04}$	$0.92^{+0.04}_{-0.04}$	96.8 (75)
		BBPL			7^{+1}_{-1}	$0.3^{+0.1}_{-0.1}$	$1.59^{+0.09}_{-0.08}$	$1.00^{+0.06}_{-0.06}$	75.8 (73)
		2BBPL	7^{+1}_{-1}	$0.2^{+0.1}_{-0.1}$	$0.07^{+0.02}_{-0.01}$	$0.2^{+0.3}_{-0.1}$	$1.51^{+0.08}_{-0.07}$	$0.93^{+0.06}_{-0.06}$	65.8 (71)
		Band							96.2 (73)
19	253.2 – 573.2	PL				$1.50^{+0.06}_{-0.06}$	$0.03^{+0.02}_{-0.02}$	14.3 (17)	

+ PL model taking all the observations together. The panels are same as in Fig. 5 that refers to the 2BB + PL model fitted at early times. In Fig. 7, similar plot is shown for the Band + BB model. In both cases, the evolution at the late phase is consistent with the previous evolution. The late time spectral evolution together with a significantly better reduced χ^2 in the high resolution data of the XRT suggests that the 2BB + PL model probably most consistently captures the overall spectral evolution of the burst.

3.3 Evidence for a second hard pulse

In case of GRBs with multiple but separable pulses, it is frequently observed that the first pulse shows a HTS evolution, followed by a jump in the peak energy during the onset of a second pulse, and then again showing a HTS evolution in the falling part of that pulse (see e.g., Ghirlanda, Nava & Ghisellini 2010; Lu et al. 2012). A very similar behaviour is seen for GRB 151006A, though the presence of a second pulse is not seen in the lightcurve. The late time spectral evolution being consistently HTS since the time of sudden jump (≥ 18 s, see Section 3.2) indicates that the second phase is probably a second pulse of the prompt emission hidden in the data. This is not readily evident probably because it is expected to be a hard pulse, where the signal is weak. In order to have a better look at the phenomenon we perform the following analysis.

We first construct the Bayesian blocks for the combined count rate data of NaI 0, 1 and 3 in 8–900 keV (see Fig. 8, upper panel). The Bayesian block approach finds the best possible way to represent a time-series data as a series of blocks or segments such that the signal underlying each block is constant within the observational error (Scargle et al. 2013). We use the dynamical programming algorithm of Scargle et al. (2013) to construct these blocks which are then over-plotted on the count rate lightcurve in Fig. 8, upper panel. During the interval shown in the Figure, we find the Bayesian blocks as -1–1 s, 1–10 s, 10–15 s and 15–24 s. With only the NaI 3 detector these blocks are -1–1 s, 1–14 s and 14–24 s. We note that a new block starts at ~ 14 –15 s which shows that the count rate flux of this bin is statistically different from the Bayesian blocks on

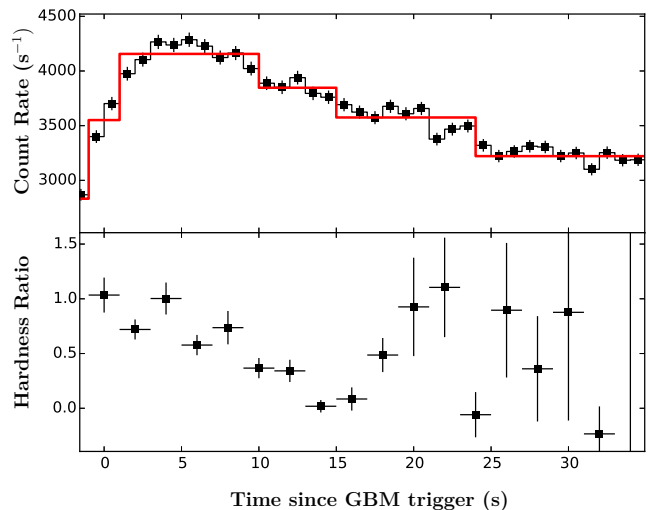


Figure 8. Upper panel: Bayesian blocks shown on the light curve of combined NaI 0, 1 and 3 in 8–900 keV. The blocks are -1–1 s, 1–10 s, 10–15 s and 15–24 s. clearly, a new block starts near the time of first detected LAT photon at ~ 18 s. Lower panel: Hardness ratio defined as the ratio of count between 500 keV–5 MeV and 200 keV–400 keV band of BGO 0. A sudden increment of hardness is apparent at ~ 18 s.

either side on the time axis. But, as the flux level of the consecutive blocks around this block decreases monotonically, there is no evidence for a new pulse in the data. However, we note from Table A1 that the peak energy at the transition time reaches a very high value ~ 5 MeV, and hence, it is unlikely that such a change will give rise to any significant pulse profile in the NaI detectors. On the other hand, the flux level of BGO detector is quite poor to carry out such analysis.

Given the high value of the peak energy, and no pulse profile with Bayesian blocks in the NaI detector, we are left with only one possibility that the pulse is hidden in the BGO data and we investi-

gate that possibility. Before proceeding, we note that there are two competing factors here: a lightcurve constructed in a wide energy band will smear out the small variations that we expect at the high energies. On the other hand, a lightcurve in a limited bandwidth suffers from the poor statistics of photon count, more so for the BGO detector and that too at a time when the photon flux is already low. This is why we used the full band of the NaI detector for the Bayesian block analysis in the first place. A more robust way to investigate it further is to study the evolution of hardness ratio (HR) rather than the count rate lightcurve in a limited band. As the HR is a ratio of count between two energy bands, the small changes in the photon count subjected to the change in spectral peak will be amplified. More importantly, if there is a smooth pulse presumably a hard one, which is not seen in the lightcurve otherwise, the HR should track that pulse profile. We use the BGO detector (the BGO 0) rather than the NaI since the peak energy reaches high values covered by the BGO energy band. On the other hand, we cannot use the LAT LLE data as it does not provide the low energy band required for this analysis. We choose the hard band as $H = 500 \text{ keV} - 5 \text{ MeV}$ and the soft band as $S = 200 \text{ keV} - 400 \text{ keV}$, and then the Hardness Ratio = H/S . We then stick to the same definition throughout. The evolution is shown in Fig. 8, lower panel. The first phase shows a HTS evolution starting with a hardness ratio of ~ 1 , reaching down to a value close to 0 until $\sim 15 \text{ s}$ and then shows a sudden jump again reaching a hardness ratio of ~ 1 , followed by another HTS evolution. The errors in the hardness ratio are larger at the later phase due to the lower flux level, but the evidence of the jump in hardness lightcurve, and a smooth pulse profile afterwards is very clear. This changeover time remarkably coincides with the onset of the unusual spectral evolution. This is exactly when the second phase of emission begins and the first LAT photon ($> 100 \text{ MeV}$) is detected. This analysis, combined with the fact that the second phase shows a very similar HTS evolution as seen in other GRBs, points towards the fact that this new energy injection is due to a second hard pulse of the prompt emission itself.

3.4 Polarization measurement – further evidence for the second pulse of prompt emission

Another piece of information about these two emission phases can be obtained from polarization measurement. If the second emission phase is a hard pulse, and we attribute polarization to the non thermal processes that produce harder spectrum, then we expect to have an enhancement of the degree of polarization in the second phase. CZTI being a pixelated detector and having a significant Compton scattering probability at energies beyond 100 keV , essentially works as a Compton polarimeter at these energies. The double pixel events within the photon tagging time window of $40 \mu\text{s}$ which satisfy the Compton kinematics are identified as valid Compton events. The validity of the Compton event selection and the polarization measurement capability of CZTI have been established by detailed simulation and experimental studies during ground calibration of CZTI (Chattopadhyay et al. 2014; Vadawale et al. 2015). The first onboard validation of CZTI polarimetry was obtained with the detection of polarization of GRB 160131A (Vadawale et al. 2016) and GRB 151006A (Rao et al. 2016). GRB151006A, though is moderately bright for X-ray polarization measurement, a hint of polarization is seen with an estimated polarization degree $> 90\%$ with a detection significance of 1.5σ (68% confidence level with 1 parameter of interest). Since our spectroscopic analysis shows that there could be two distinct phases of emission, we tried to explore polarization measurement in these two sectors using the CZTI data.

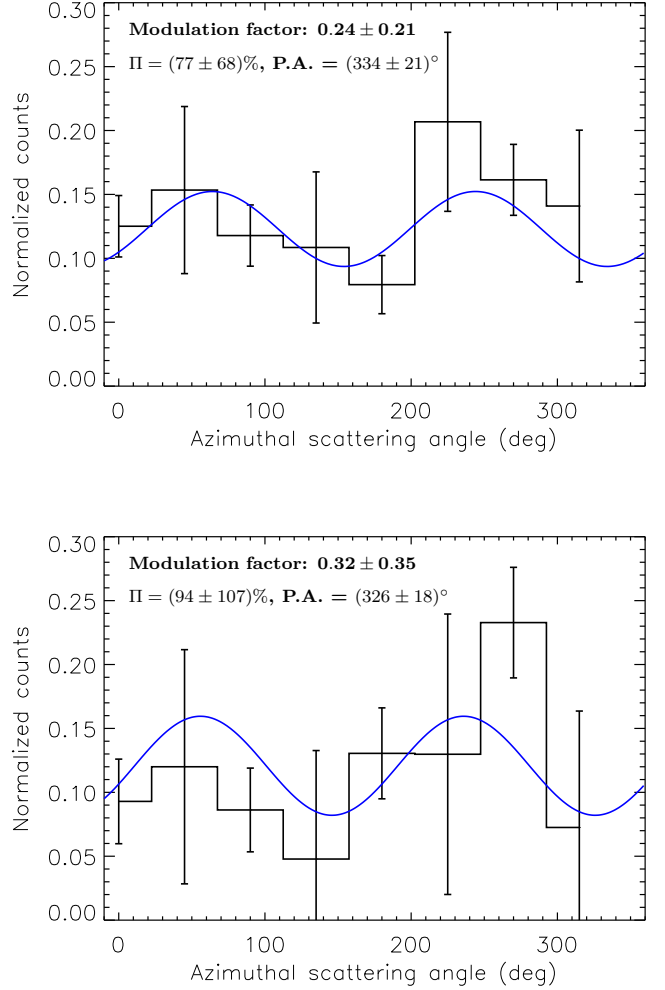


Figure 9. Modulation curves for GRB 151006A in two phases: 0–16 s (upper panel) and 16–33 s (lower panel). The modulation curve is obtained after geometrically correcting the raw azimuthal angle histogram by normalizing with respect to a simulated unpolarized distribution for a similar spectra and off-axis detection angle (Rao et al. 2016). The blue solid line is the $\cos^2 \phi$ fit to the modulation curve. The fitted modulation factor, polarization fraction (Π) and polarization angle (P. A.) are shown in the inset of the respective panels, with errors estimated at 68% confidence level (see text for details).

Fig. 9 shows the modulation curves for these two time bins in $100 - 350 \text{ keV}$, where the blue solid line is the sinusoidal fit to the observed distribution of azimuthal angle of scattering.

In order to estimate the polarization fractions, we did detailed Geant 4 simulations (Agostinelli et al. 2003) using *Astrosat* mass model which includes all the instruments of *Astrosat* along with the complete satellite structure. We employ the fitted spectroscopic models to simulate the energy distribution of the incident photons in Geant 4 to obtain the modulation factors for 100% polarized beam (μ_{100}) which are then used to estimate the polarization fractions ($P = \mu/\mu_{100}$) in two phases, 0–16 s and 16–32 s. Estimated polarization fractions are 77% and 94% with 1σ detection significance at polarization angles 334° and 325° respectively in these two phases. The detection significance of polarization has reduced significantly compared to the initial report of polarization for GRB 151006A (Rao et al. 2016) which is expected due to reduced number of events in the individual phases. Though fraction and angle

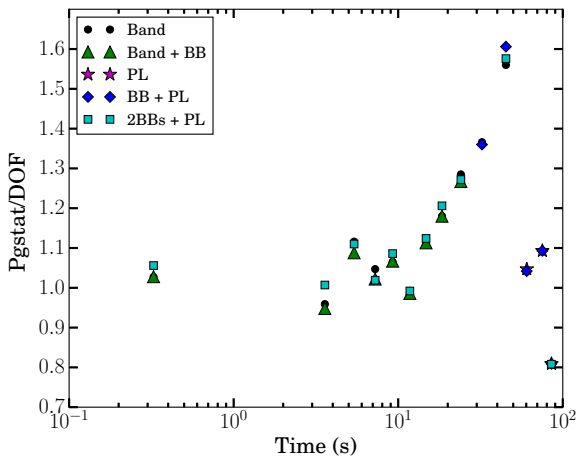


Figure 10. The PGStat/dof of all the models are shown.

of polarization are poorly constrained in both the time sectors, the measured values do not show any decrement of polarization. In the multi-component models with thermal and non thermal parts, it is suggested that the thermal emission dominates in the first part while the non thermal processes become important at the later stage (e.g., González et al. 2003). Attributing the polarization to the non thermal processes, the above evolution is consistent with the expected behaviour for such models. Hence, there is a hint of multi-component spectra in the data.

It is important to note that the polarization degree in the afterglow phase found by optical measurements so far show a pretty low value ($\lesssim 10\%$) and it is expected to reduce further as the afterglow proceeds, see e.g., Greiner et al. (2003); Mundell et al. (2007). This appears to be due to the fact that the magnetic field during the afterglow phase is mostly generated by turbulence and therefore has a random orientation, having only a small coherence length. This is in contrast with the prompt emission phase, where measurements show a high degree of polarization ($\sim 40 - 80\%$) which can be achieved by an ordered magnetic field, see Waxman (2003). Though a different mechanism is possible to achieve a high degree of polarization of the prompt emission, the important point is that such high values are not seen in the afterglow phase. Our measurement is consistent with a high value, and though the statistics is poor the measured values in the two phase do not contradict the interpretation that we are most probably observing the prompt emission extending out to the second phase. Hence, the data is indicative of a second hard pulse rather than the onset of an afterglow phase.

3.5 Comparison between the models

We then compare the different models based on their goodness of fit. The PG-Stat/dof of all the models in different time bins are shown in Fig. 10. We note that all the models have very similar PG-Stat. Thus, making the judgment of the best model is quite indecisive. We then use Bayesian inference criteria (BIC) to see whether the more complicated models are indeed required by statistics (e.g., Wang et al. 2017). The BIC is defined as $-2 \ln \mathcal{L} + k \ln(\nu + k)$, where $-2 \ln \mathcal{L}$ is log likelihood, k is the number of free parameters and ν is the degrees of freedom. In Table 4, we show the BIC values and the preferred models.

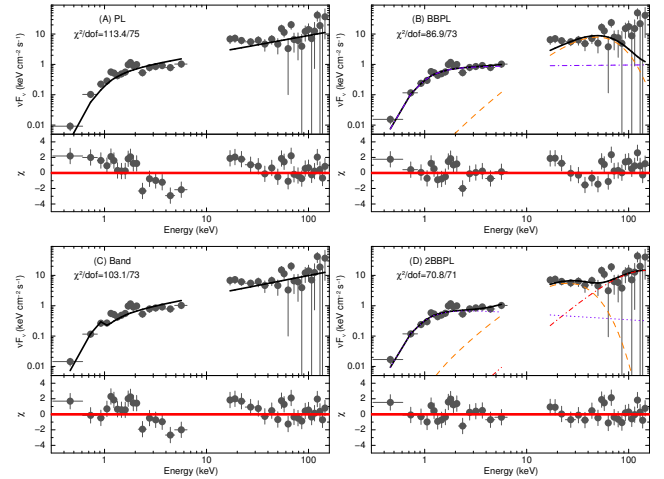


Figure 11. Spectral fitting of the joint BAT and XRT data with PL, BB + PL, Band and 2BB + PL models for the late time bin 15. The data and residual are shown by grey filled circles. The high energy blackbody, low energy blackbody (or the blackbody for the BB + PL model), the power law and the total model, are shown by red dot-dashed line, orange dashed line, violet dotted line and thick black line, respectively.

Table 4. BIC values and preferred model

#	$-2 \ln \mathcal{L}$ (BIC)				Preferred
	Band	Band+BB	2BB+PL		
1	489.8 (514.5)	488.1 (525.1)	501.7 (538.7)		Band
2	457.2 (481.9)	450.4 (525.1)	478.3 (515.3)		Band
3	532.3 (557.0)	517.0 (554.0)	527.4 (564.4)		Band+BB
4	499.2 (523.9)	485.5 (522.5)	483.8 (520.8)		2BB+PL
5	507.8 (532.5)	506.7 (543.7)	515.8 (552.8)		Band
6	471.2 (495.9)	468.3 (505.3)	471.1 (508.1)		Band
7	529.5 (554.2)	528.6 (565.6)	534.1 (571.1)		Band
8	574.9 (599.7)	572.5 (609.7)	578.1 (615.3)		Band
9	612.8 (637.5)	601.9 (638.9)	604.2 (641.2)		Band
10	640.5 (665.1)				Band
11	747.4 (772.1)		751.1 (788.2)		Band
	BBPL	BBCPL	PL		
12	1497 (1526)	1498 (1534)	1505 (1520)		PL
13	1571 (1600)	1566 (1602)	1573 (1587)		PL
14	1162 (1191)	1162 (1199)	1165 (1179)		PL
	BBPL	2BB+PL	PL		
15	86.9 (104.3)	70.8 (96.9)	113.4 (122.1)		2BB+PL
16	77.8 (95.2)	70.4 (96.5)	88.9 (97.6)		BBPL/2BBPL
17	84.9 (102.3)	72.8 (98.9)	89.5 (98.2)		PL/2BBPL
18	75.8 (93.2)	65.8 (91.9)	96.8 (105.5)		2BB+PL

We note that in the initial bins where we use the *Fermi* data, the Band function is the preferred model. This signifies that the data is consistent with the Band function and a more complicated model is not statistically required. There are only two exceptions, Bin 3 and 4. In the former Band + BB is the preferred model, while in the later the 2BB + PL is the preferred model. At the later phase, we see even the PL is the preferred model and the other complicated models are not statistically required. Our result clearly shows the limitations of a background dominated low resolution detector.

However, in the late phase, though we have lower count rate, the signal to noise of the data is improved due to both BAT and XRT and we have good resolution of the XRT. We see a preference for the 2BBPL model in the data at late phase. From Table 3, we also see that the Band function is not preferred. In fact, we could not constrain the peak energy, and it signifies that the spectral shape is not a Band function.

In Fig. 11, we show the spectral fit and residuals of the PL, BB + PL, Band and 2BB + PL model fit for bin 15. Note that for the PL fit the slope at lower and higher energies do not match which is clearly indicated by the deviation of the residual in the opposite direction of the zero line. For the BBPL model, this is improved, but then we find large residual on the both sides of the blackbody peak. The Band function fares no better than the PL model and has a similar residual. All the curvatures in the spectrum are consistently taken care by the 2BB + PL model.

4 CONCLUSIONS AND DISCUSSION

Single pulse bursts have been carefully studied using time resolved spectroscopy, as it is generally assumed to alleviate the issue of pulse overlapping which hinders our understanding of spectral evolution of GRB with time. GRB 151006A is a single pulse burst in different energy bands and thereby is an ideal one for time resolved spectroscopy. In general, such bursts exhibit a HTS spectral peak evolution. However, the current analysis of GRB 151006A shows an unexpected behaviour of change in trend from HTS evolution to increasing spectral peak with time, after a few seconds from the burst trigger. Coincidentally, this rise is observed after the arrival of LAT photons (> 100 MeV). Such a dramatic change in the spectral behaviour for single pulse burst is observed for the first time. This new injection of energy does not show any additional pulse in the counts light curve. Thus, this cautions us that a single pulse need not always suggest a HTS spectral peak evolution and that there may be other pulses hidden in the light curve profile.

It is important to notice that high energy emission is often delayed and generally modelled with powerlaw appearing in the spectrum at late times (e.g., González et al. 2003; Ackermann et al. 2013). This can potentially change the behaviour of the spectral evolution we report here. However, we have tested that a powerlaw with Band function is not statistically required for Bin 8 and 11. This is apparent from the spectral shape in Fig. 3. GRB 151006A is not among the high-fluence LAT class (cf. Ackermann et al. 2013), and for several such cases the spectrum is found to be well fitted with Band function only and no powerlaw is required.

In order to show that the E_p variation is physical and not due to single peak Band function, we also tried models with two peaks i.e., Band + BB and 2BB + PL, and re-confirm the spectral variation. The analysis also presents one of the key issues in current GRB spectral analysis i.e., a preferred model cannot be decided based only on statistics. Though in the later part the 2BB + PL model seems to be a better fit. In Basak & Rao (2015a) the spectral components of this model is proposed to originate in a spine-sheath jet (Ramirez-Ruiz, Celotti & Rees 2002; Zhang, Woosley & MacFadyen 2003; Zhang, Woosley & Heger 2004, see Iyyani et al. 2015 for an alternative explanation). The blackbody radiations are produced at the two photospheres. In addition, photons crossing the boundary layer of the spine-sheath structure are on an average Compton up-scattered and hence form a high energy power-law spectrum. Further non thermal processes can occur due to synchrotron emission at a higher radial distance. These photons

are naturally delayed with respect to the photons produced by thermal and non thermal processes stated above. Hence, the second phase in this scenario is probably an onset of the delayed emission phase. We note here that though the second phase starts after ~ 18 s, the pulse can have a much lower start time, which is hidden in the falling part of the first pulse. Hence, an actual delay of this phase can be much smaller, though remains undetermined.

Recently, Moretti & Axelsson (2016) reported a rise in the high energy spectral peak with time, for the first LAT detected GRB 080825C, a multi-pulse burst (Abdo et al. 2009), when it was re-analysed including the LLE data. This points out the significance of LLE emission detections which can be crucial in constraining the high energy spectral behaviour of GRB spectra. The interesting part of our observation is that the increasing behaviour is seen in an otherwise single pulse. The new injection of energy may be associated with a second pulse of emission in the prompt phase which brings about a dynamical change in the behaviour of the radiation process, or it may be an overlap of the onset of afterglow (emission from a different region) with the prompt emission, which then significantly dominates the high energy and thereby making the prompt emission indiscernible in the spectrum. We note that the α values of Band function to be consistent with slow cooling synchrotron radiation in the beginning of the burst (< -0.67) and gets softer with time approaching the fast cooling index ($\alpha = -1.5$). If the new energy injection is due to a second pulse in the prompt emission, we may be observing a transition in the microphysical parameters related to the synchrotron radiation, such as strength or structure of magnetic fields, fraction of energy injected into electrons, radiation efficiency etc (Daigne & Mochkovitch (1998)), causing the transformation from slow to fast cooling of electrons, see Iyyani et al. (2016). Since this transformation is observed to be sudden, it perhaps indicate the onset of a second pulse with a different source parameter. For the afterglow scenario, such emission has been mostly modelled using a power law (Ackermann et al. 2013; Kumar & Barniol Duran 2009; Ghisellini et al. 2010). However, we note a definite spectral curvature at late times and the detection of LAT emission is less significant and not many photons are detected. Our analysis with Bayesian block and evolution study of the hardness ratio also points towards the former scenario i.e., a new hard pulse hidden in the data.

Finally, the inability of determining the best model based on statistics also summons for constraining observations like polarization. This can potentially characterize various radiation processes leading to the observed emission as well as in revealing the structure and strength of magnetic fields of emitting region. This can in turn be an invaluable input in enhancing our understanding of shock physics as well as the content of GRB jets. A significant polarization detection requires high photon statistics and lack of this has actually prevented the CZTI instrument onboard *Astrosat* in constraining the polarization measurement for GRB 151006A. The current measurement hints a moderately high polarization, however, with low significance, and thereby is consistent with nearly all model predictions. However, the capability demonstrated by CZTI, offers a promising era of polarization detections above 100 keV and also its time dependent study, in case of brighter GRBs.

ACKNOWLEDGMENTS

We gratefully acknowledge the referee for comments on reshaping the paper. This publication uses data from the *Astrosat* mission of the Indian Space Research Organisation (ISRO), archived at the

Indian Space Science Data Centre (ISSDC). CZT-Imager is built by a consortium of Institutes across India including Tata Institute of Fundamental Research, Mumbai, Vikram Sarabhai Space Centre, Thiruvananthapuram, ISRO Satellite Centre, Bengaluru, Inter University Centre for Astronomy and Astrophysics, Pune, Physical Research Laboratory, Ahmedabad, Space Application Centre, Ahmedabad: contributions from the vast technical team from all these institutes are gratefully acknowledged. This research has made use of data obtained through the HEASARC Online Service, provided by the NASA/GSFC, in support of NASA High Energy Astrophysics Programs. RB is a stipendiary of START program of the Polish Science Foundation (2016) and supported by Polish National Science Centre grants 2013/08/A/ST9/00795, 2013/10/M/ST9/00729 and 2015/18/A/ST9/00746.

REFERENCES

- Abdo A. A. et al., 2009, *ApJ*, 707, 580
 Ackermann M. et al., 2013, *ApJS*, 209, 11
 Agostinelli S. et al., 2003, *Nuclear Instruments and Methods in Physics Research A*, 506, 250
 Atwood W. B. et al., 2009, *ApJ*, 697, 1071
 Axelsson M. et al., 2012, *ApJ*, 757, L31
 Band D. et al., 1993, *ApJ*, 413, 281
 Basak R., Rao A. R., 2014, *MNRAS*, 442, 419
 Basak R., Rao A. R., 2015a, *ApJ*, 812, 156
 Basak R., Rao A. R., 2015b, *ApJ*, 807, 34
 Beloborodov A. M., 2010, *MNRAS*, 407, 1033
 Beloborodov A. M., 2011, *ApJ*, 737, 68
 Beloborodov A. M., 2013, *ApJ*, 764, 157
 Bhalerao V., Bhattacharya D., Rao A. R., Vadawale S., 2015, *GRB Coordinates Network*, 18422
 Burgess J. M. et al., 2014, *ApJ*, 784, 17
 Burrows D. N. et al., 2005, *Space Science Reviews*, 120, 165
 Chattopadhyay T., Vadawale S. V., Rao A. R., Sreekumar S., Bhattacharya D., 2014, *Experimental Astronomy*, 37, 555
 Coburn W., Boggs S. E., 2003, *Nature*, 423, 415
 Crider A. et al., 1997, *ApJ*, 479, L39
 Cummings J. R. et al., 2015, *GRB Coordinates Network*, 18410
 Daigne F., Mochkovitch R., 1998, *MNRAS*, 296, 275
 Evans P. A. et al., 2009, *MNRAS*, 397, 1177
 Gehrels N. et al., 2004, *ApJ*, 611, 1005
 Ghirlanda G., Celotti A., Ghisellini G., 2003, *A&A*, 406, 879
 Ghirlanda G., Nava L., Ghisellini G., 2010, *A&A*, 511, A43
 Ghisellini G., Celotti A., 1999, *ApJ*, 511, L93
 Ghisellini G., Ghirlanda G., Nava L., Celotti A., 2010, *MNRAS*, 403, 926
 Ghisellini G., Lazzati D., Celotti A., Rees M. J., 2000, *MNRAS*, 316, L45
 Giannios D., 2012, *MNRAS*, 422, 3092
 Goldstein A., Preece R. D., Mallozzi R. S., Briggs M. S., Fishman G. J., Kouveliotou C., Paciesas W. S., Burgess J. M., 2013, *ApJS*, 208, 21
 Golenetskii S. et al., 2015, *GRB Coordinates Network*, 18413
 González M. M., Dingus B. L., Kaneko Y., Preece R. D., Dermer C. D., Briggs M. S., 2003, *Nature*, 424, 749
 Götz D., Covino S., Fernández-Soto A., Laurent P., Bošnjak Ž., 2013, *MNRAS*, 431, 3550
 Götz D., Laurent P., Lebrun F., Daigne F., Bošnjak Ž., 2009, *ApJ*, 695, L208
 Granot J., Königl A., 2003, *ApJ*, 594, L83
 Greiner J., Burgess J. M., Savchenko V., Yu H.-F., 2016, *ArXiv e-prints*
 Greiner J. et al., 2003, *Nature*, 426, 157
 Gruber D. et al., 2014, *ApJS*, 211, 12
 Guiriec S. et al., 2011, *ApJ*, 727, L33
 Guiriec S. et al., 2013, *ApJ*, 770, 32
 Hakkila J., Preece R. D., 2014, *ApJ*, 783, 88
 Iyyani S. et al., 2015, *MNRAS*, 450, 1651
 Iyyani S., Ryde F., Axelsson M., Burgess J. M., et al., 2013, *MNRAS*, 433, 2739
 Iyyani S., Ryde F., Burgess J. M., Pe'er A., Bégué D., 2016, *MNRAS*, 456, 2157
 Kalemci E., Boggs S. E., Kouveliotou C., Finger M., Baring M. G., 2007, *ApJS*, 169, 75
 Kaneko Y., Preece R. D., Briggs M. S., Paciesas W. S., Meegan C. A., Band D. L., 2006, *ApJS*, 166, 298
 Kocevski D., Barthelmy S. D., Evans P. A., Page K. L., Sbarufatti B., 2015, *GRB Coordinates Network*, 18398
 Kumar P., Barniol Duran R., 2009, *MNRAS*, 400, L75
 Kumar P., Zhang B., 2015, *Phys. Rep.*, 561, 1
 Lazzati D., Rossi E., Ghisellini G., Rees M. J., 2004, *MNRAS*, 347, L1
 Liang E., Kargatis V., 1996, *Nature*, 381, 49
 Lu R.-J., Wei J.-J., Liang E.-W., Zhang B.-B., Lü H.-J., Lü L.-Z., Lei W.-H., Zhang B., 2012, *ApJ*, 756, 112
 Lundman C., Pe'er A., Ryde F., 2013, *MNRAS*, 428, 2430
 Lundman C., Pe'er A., Ryde F., 2014, *MNRAS*, 440, 3292
 Lundman C., Vurm I., Beloborodov A. M., 2016, *ArXiv e-prints*
 McGlynn S. et al., 2007, *A&A*, 466, 895
 Meegan C. et al., 2009, *ApJ*, 702, 791
 Mészáros P., 2006, *Reports on Progress in Physics*, 69, 2259
 Moretti E., Axelsson M., 2016, *MNRAS*, 458, 1728
 Mundell C. G. et al., 2007, *Science*, 315, 1822
 Nakar E., Piran T., Waxman E., 2003, *J. Cosmology Astropart. Phys.*, 10, 005
 Ohno M., Bissaldi E., Vianello G., Kocevski D., Longo F., 2015, *GRB Coordinates Network*, 18406
 Pe'er A., 2015, *Advances in Astronomy*, 2015, 907321
 Pe'er A., Mészáros P., Rees M. J., 2005, *ApJ*, 635, 476
 Piran T., 2004, *Reviews of Modern Physics*, 76, 1143
 Preece R. D., Briggs M. S., Mallozzi R. S., Pendleton G. N., Paciesas W. S., Band D. L., 1998, *ApJ*, 506, L23
 Ramirez-Ruiz E., Celotti A., Rees M. J., 2002, *MNRAS*, 337, 1349
 Rao A. R. et al., 2016, *ApJ*, 833, 86
 Rees M. J., Mészáros P., 1994, *ApJL*, 430, L93
 Rees M. J., Mészáros P., 2005, *ApJ*, 628, 847
 Roberts O. J., Meegan C., 2015, *GRB Coordinates Network*, 18404
 Rutledge R. E., Fox D. B., 2004, *MNRAS*, 350, 1288
 Ryde F., 2004, *ApJ*, 614, 827
 Ryde F., 2005, *ApJ*, 625, L95
 Ryde F., Pe'er A., 2009, *ApJ*, 702, 1211
 Sari R., Piran T., Narayan R., 1998, *ApJL*, 497, L17
 Scargle J. D., Norris J. P., Jackson B., Chiang J., 2013, *ApJ*, 764, 167
 Tavani M., 1996, *ApJ*, 466, 768
 Vadawale S. V., Chattopadhyay T., Mithun N. P. S., Rao A. R., Bhattacharya D., Bhalerao V., 2016, *GRB Coordinates Network*, 19011
 Vadawale S. V., Chattopadhyay T., Rao A. R., Bhattacharya D., Bhalerao V. B., Vaghshette N., Pawar P., Sreekumar S., 2015, *A&A*, 578, A73
 Wang Y.-Z. et al., 2017, *ApJ*, 836, 81
 Waxman E., 2003, *Nature*, 423, 388
 Wigger C., Hajdas W., Arzner K., Güdel M., Zehnder A., 2004, *ApJ*, 613, 1088
 Yonetoku D. et al., 2012, *ApJ*, 758, L1
 Yonetoku D. et al., 2011, *ApJ*, 743, L30
 Yoshida A. et al., 2015, *GRB Coordinates Network*, 18475
 Zhang B., 2014, *International Journal of Modern Physics D*, 23, 30002
 Zhang W., Woosley S. E., Heger A., 2004, *ApJ*, 608, 365
 Zhang W., Woosley S. E., MacFadyen A. I., 2003, *ApJ*, 586, 356

APPENDIX A: TABLE OF SPECTRAL ANALYSIS

Here we have reported the parameters obtained from time resolved spectral analysis using the Band + BB (Table A1), 2BB+PL (Table A2) and BB+PL (Table A3). In Table A3, we also show the Pg-stat/dof of two more models i.e power law (PL) and blackbody + cutoff power law (BB + CPL), for comparison.

Table A1. Parameters of time resolved spectral fitting with Band + BB model in bin 1–9

Bin #	Time interval (s)	kT (keV)	N_{BB}	α (keV)	β	E_{peak} (keV)	N_{Band} (10^{-3})	PG-Stat (dof)
1	-2.0 – 2.7	22^{+22}_{-8}	$0.12^{+0.08}_{-0.08}$	$-0.85^{+0.06}_{-0.05}$	$-2.8^{+0.2}_{-0.2}$	3220^{+770}_{-704}	$3.1^{+0.2}_{-0.2}$	488.1 (475)
2	2.7 – 4.5	14^{+2}_{-2}	$0.61^{+0.11}_{-0.11}$	$-1.05^{+0.06}_{-0.04}$	$-2.6^{+0.2}_{-0.2}$	2892^{+7099}_{-1919}	$8.9^{+0.4}_{-0.4}$	450.4 (475)
3	4.5 – 6.3	23^{+2}_{-2}	$1.22^{+0.15}_{-0.16}$	$-1.12^{+0.05}_{-0.06}$	$-2.9^{+0.2}_{-0.4}$	2281^{+7709}_{-699}	$8.3^{+0.4}_{-0.4}$	517.0 (475)
4	6.3 – 8.2	28^{+3}_{-2}	$1.42^{+0.20}_{-0.16}$	$-1.34^{+0.06}_{-0.03}$	$-2.8^{+0.3}_{-0.6}$	4893^{+2193}_{-1717}	$7.8^{+0.5}_{-0.3}$	485.5 (475)
5	8.2 – 10.3	12^{+6}_{-4}	$0.25^{+0.23}_{-0.16}$	$-1.16^{+0.14}_{-0.04}$	$-2.4^{+0.1}_{-0.1}$	986^{+1135}_{-365}	$10.3^{+0.5}_{-0.5}$	506.7 (475)
6	10.3 – 13.2	12^{+4}_{-2}	$0.34^{+0.21}_{-0.20}$	$-1.10^{+0.17}_{-0.13}$	$-2.4^{+0.1}_{-0.2}$	610^{+541}_{-221}	$8.8^{+0.1}_{-0.1}$	468.3 (475)
7	13.2 – 16.3	$10^{+20}_{-\infty}$	$0.19^{+0.20}_{-\infty}$	$-1.09^{+0.22}_{-0.18}$	$-2.3^{+0.1}_{-0.2}$	412^{+374}_{-158}	$9.6^{+0.2}_{-0.2}$	528.6 (475)
8 ^(a)	16.3 – 20.6	33^{+4}_{-4}	$0.74^{+0.12}_{-0.10}$	$-1.50^{+0.05}_{-0.03}$	$-3.0^{+0.2}_{-0.9}$	5274^{+3102}_{-4311}	$4.2^{+0.3}_{-0.1}$	572.5 (485)
9	20.6 – 27.5	19^{+3}_{-3}	$0.39^{+0.06}_{-0.06}$	$-1.42^{+0.03}_{-0.03}$	$-3.5^{+0.7}_{-\infty}$	5078^{+2370}_{-2228}	$3.1^{+0.2}_{-0.2}$	601.9 (475)

Note: (a) Including LAT data

Table A2. Parameters of time resolved spectral fitting with 2BB + PL model

Bin #	Time interval (s)	kT_{h} (keV)	N_{h}	kT_{l} (keV)	N_{l}	Γ	N_{Γ}	PG-Stat (dof)
1	-2.0 – 2.7	730^{+103}_{-91}	23^{+4}_{-4}	89^{+18}_{-16}	$2.6^{+0.8}_{-0.6}$	$1.62^{+0.03}_{-0.03}$	2^{+1}_{-1}	501.7 (475)
2	2.7 – 4.5	302^{+70}_{-59}	19^{+4}_{-4}	36^{+7}_{-6}	$2.5^{+0.5}_{-0.5}$	$1.72^{+0.03}_{-0.03}$	10^{+2}_{-2}	478.3 (475)
3	4.5 – 6.3	305^{+88}_{-78}	17^{+6}_{-4}	30^{+3}_{-3}	$3.0^{+0.3}_{-0.3}$	$1.85^{+0.05}_{-0.04}$	12^{+3}_{-3}	527.4 (475)
4	6.3 – 8.2	424^{+94}_{-104}	19^{+6}_{-5}	32^{+2}_{-2}	$3.0^{+0.3}_{-0.3}$	$1.85^{+0.04}_{-0.04}$	16^{+3}_{-3}	483.8 (475)
5	8.2 – 10.3	142^{+37}_{-27}	7^{+1}_{-1}	25^{+6}_{-5}	$1.6^{+0.4}_{-0.3}$	$1.88^{+0.05}_{-0.04}$	17^{+4}_{-4}	515.8 (475)
6	10.3 – 13.2	86^{+13}_{-11}	5^{+1}_{-1}	16^{+2}_{-2}	$1.0^{+0.2}_{-0.2}$	$1.88^{+0.06}_{-0.05}$	10^{+4}_{-3}	471.1 (475)
7	13.2 – 16.3	82^{+21}_{-15}	4^{+1}_{-1}	18^{+5}_{-4}	$1.0^{+0.3}_{-0.2}$	$1.92^{+0.07}_{-0.06}$	13^{+4}_{-3}	534.1 (475)
8 ^(a)	16.3 – 20.6	217^{+70}_{-53}	4^{+2}_{-1}	30^{+4}_{-3}	$1.4^{+0.2}_{-0.2}$	$1.99^{+0.08}_{-0.06}$	16^{+5}_{-3}	578.1 (484)
9	20.6 – 27.5	592^{+179}_{-397}	10^{+4}_{-7}	26^{+3}_{-4}	$1.0^{+0.1}_{-0.1}$	$1.97^{+0.07}_{-0.05}$	11^{+3}_{-2}	604.2 (475)
11 ^(a)	37.1 – 53.2	448^{+181}_{-229}	5^{+2}_{-2}	33^{+8}_{-6}	$0.4^{+0.1}_{-0.1}$	$1.98^{+0.06}_{-0.06}$	5^{+1}_{-1}	751.1 (477)
14	82.7 – 88.1	54^{+40}_{-20}	$0.3^{+0.2}_{-0.2}$	6^{+5}_{-2}	$0.06^{+0.04}_{-0.04}$	$1.83^{+0.13}_{-0.11}$	$1.1^{+0.1}_{-0.1}$	1160.4 (1436)

Note: (a) Including LAT data

Table A3. Parameters of time resolved spectral fitting with BB + PL model in bin 10–14. Bin 12–14 have a simultaneous coverage with the XRT.

Bin #	Time interval (s)	kT (keV)	N_{kT}	Γ	N_{Γ}	PG-Stat (dof)	PG-Stat(dof) _{PL}	PG-Stat (dof) _{BBCPL}
10	27.5 – 37.1	28^{+8}_{-7}	$0.2^{+0.1}_{-0.1}$	$1.52^{+0.05}_{-0.05}$	$2.3^{+0.6}_{-0.5}$	638.1 (469)	642.1 (471)	640.1 (468)
11	37.1 – 53.2	85^{+23}_{-19}	$1.1^{+0.2}_{-0.2}$	$1.98^{+0.05}_{-0.05}$	$5.6^{+1.2}_{-1.0}$	769.3 (479)	830.4 (480)	757.1 (478)
12	53.2 – 67.7	13^{+4}_{-3}	$0.11^{+0.04}_{-0.04}$	$1.41^{+0.02}_{-0.02}$	$0.75^{+0.03}_{-0.03}$	1497.1 (1438)	1505.4 (1440)	1498.1 (1437)
13	67.7 – 82.6	11^{+6}_{-4}	$0.05^{+0.04}_{-0.04}$	$1.55^{+0.03}_{-0.03}$	$1.09^{+0.04}_{-0.04}$	1571.1 (1438)	1572.7 (1440)	1565.7 (1437)
14	82.6 – 88.1	50^{+49}_{-24}	$0.2^{+0.2}_{-0.1}$	$1.73^{+0.08}_{-0.08}$	$1.04^{+0.08}_{-0.08}$	1162.2 (1438)	1164.8 (1440)	1162.3 (1437)